Understanding microstructural changes of a one-part geopolymer exposed to CO2 for geological carbon storage application – An experimental and numerical investigation

Gupta, Mayank; Hajiabadi, Seyed Hasan; Aghabeyk, Farnaz; Chen, Yun; van Noort, Reinier; Khalifeh, Mahmoud; Ye, Guang

DOI
10.1016/j.ccst.2025.100466

Publication date
2025

Document Version
Final published version

Published in
Carbon Capture Science and Technology

Citation (APA)
Gupta, M., Hajiabadi, S. H., Aghabeyk, F., Chen, Y., van Noort, R., Khalifeh, M., & Ye, G. (2025). Understanding microstructural changes of a one-part geopolymer exposed to CO2 for geological carbon storage application – An experimental and numerical investigation. *Carbon Capture Science and Technology*, *16*, Article 100466. https://doi.org/10.1016/j.ccst.2025.100466

16 (2025) 100466

Contents lists available at ScienceDirect

Carbon Capture Science & Technology

journal homepage: www.elsevier.com/locate/ccst

Full Length Article

Understanding microstructural changes of a one-part geopolymer exposed to CO_2 for geological carbon storage application – An experimental and numerical investigation

Mayank Gupta [a,*], Seyed Hasan Hajiabadi [b], Farnaz Aghabeyk [a], Yun Chen [a], Reinier van Noort [c], Mahmoud Khalifeh [b], Guang Ye [a]

[a] Department of Materials, Mechanics, Management & Design, Delft University of Technology, Delft, 2628 CN, the Netherlands
[b] Department of Energy and Petroleum Engineering, University of Stavanger, Stavanger 4036, Norway
[c] Department of Reservoir Technology, Institute for Energy Technology, Postbox 40, 2027, Kjeller, Norway

ARTICLE INFO

Keywords:
Alkali activated materials
Reaction and transport
Geological carbon storage
Thermodynamic modeling
Microstructure

ABSTRACT

While ensuring the long-term integrity of wellbore sealants is critical for the success of geological carbon storage (GCS), the chemical degradation of conventional materials under CO_2-rich conditions remains a major challenge. This study investigates the carbonation behavior of a one-part granite-based geopolymer, integrating a novel pore-scale simulation framework with experimental validation. A new model, ReacSan, is developed to simulate CO_2 transport and carbonation reactions within the evolving microstructure of the geopolymer under GCS-relevant conditions. The framework incorporates CO_2 dissolution using the Redlich–Kwong equation of state, gel dissolution via transition state theory, ion transport using the Lattice Boltzmann Method, and chemical reactions through thermodynamic modeling. The model was validated through experiments exposing equivalent geopolymer samples to CO_2 under in-situ conditions. The experimentally observed rapid carbonation, leading to a decrease in pore fluid pH and the precipitation of $CaCO_3$ matched the numerical simulations well, demonstrating the ability of the novel ReacSan framework to capture both temporal and spatial variations in the microstructure and carbonation mechanisms of alkali-activated materials (AAMs) exposed to supercritical CO_2. Based on the demonstrated validity of the model, the model is capable of providing detailed predictions of carbonation progression of AAMs or any other sealants over longer time- and length-scales required to ensure long-term GCS integrity.

1. Introduction

The increasing concentration of greenhouse gases, particularly carbon dioxide (CO_2), in the atmosphere has necessitated the development of effective strategies for mitigating climate change (Echevarria Huaman and Jun, 2014; Wennersten et al., 2015). Carbon Capture and Storage (CCS) has emerged as a critical component in this effort, with the Intergovernmental Panel on Climate Change (IPCC) highlighting the potential of geological carbon storage (GCS) to stabilize atmospheric CO_2 levels (Stocker, 2014; Field and Barros, 2014). GCS involves the injection and storage of captured CO_2 in underground geological reservoirs such as depleted oil fields and saline aquifers (Liu et al., 2025; Liu et al., 2025). However, the long-term success of this approach heavily depends on the integrity of wellbore sealants, which are crucial for preventing CO_2 leakage over extended periods (Iyer et al., 2022; Bai et al., 2016; Hajiabadi et al., 2023; Kiran et al., 2017). Conventional wellbore sealants, predominantly composed of Ordinary Portland Cement (OPC), face significant challenges in CO_2-rich environments. OPC is prone to chemical degradation and brittle mechanical failure under such conditions, leading to increased porosity and permeability, which compromise its sealing effectiveness (Raza et al., 2015; Barlet-gouedard et al., 2009; Turner and Collins, 2013). These limitations have driven research into alternative materials, including calcium sulfoaluminate cement, calcium aluminate cement, and alkali-activated materials. Among the latter, geopolymers have shown particular promise due to their superior resistance to acidic environments, enhanced durability, and adaptability to harsh conditions (Nasvi et al., 2016; Nasvi et al., 2014; Bakharev, 2005; Ahmad et al., 2020).

* Corresponding author.
E-mail address: mayank.gupta.civ13@iitbhu.ac.in (M. Gupta).

https://doi.org/10.1016/j.ccst.2025.100466
Received 20 June 2025; Received in revised form 9 July 2025; Accepted 10 July 2025
Available online 10 July 2025

Recently developed rock-based geopolymers, incorporating materials such as granite and aplite, have gained attention for their suitability in downhole applications for GCS and H_2S rich environments (Khalifeh et al., 2017; van Noort et al., 2024). These materials exhibit desirable properties, including favorable setting behavior, low permeability, strong bonding with steel and geological formations, superior mechanical performance (higher strength-to-modulus ratios), minimal chemical shrinkage, and compatibility with oil-based drilling fluids (Hajiabadi et al., 2023; Eid et al., 2021; Hajiabadi et al., 2024). In addition, their widespread availability, cost-effectiveness, and low carbon footprint underscore their potential as a sustainable alternative to traditional cementitious materials, making them particularly promising for large-scale adoption in GCS projects.

The work presented here focuses on one such geopolymer, a one-part formulation based on granite, containing slag, micro-silica, K_2SiO_3, and KOH as its constituents. The main reaction products in this complex system are sodium/potassium aluminosilicate hydrates (N, K)-A-S-H). The frequent co-existence of calcium aluminosilicate hydrates (C-A-S-H) with (N, K)-A-S-H gels has been shown to significantly enhance their mechanical properties (Hajiabadi et al., 2023). Furthermore, micro-silica aids the geopolymerization process by optimizing the Si/Al ratio. This adjustment promotes the formation of critical nucleation sites, leading to a significant reduction in the permeability of geopolymers (Hajiabadi et al., 2025; Hajiabadi et al., 2023).

This geopolymer was also engineered to have a relatively low calcium content, to ensure reduced reactivity and greater stability under CO_2-rich conditions. Experimental studies have demonstrated this by exposing samples to both clean and impure CO_2 in the presence of water (van Noort et al., 2025; van Noort et al., 2025). While some Ca-leaching occurs, the structural integrity remains largely unaffected, and degradation is negligible under wet supercritical CO_2 conditions (van Noort et al., 2025). Hajiabadi et al. conducted microstructural analyses, including XRD, SEM-EDS, and FTIR, revealing the formation of distinct zones within CO_2-exposed geopolymers, such as a leaching front, carbonated zone, carbonation front, and unaltered zone. Increased crystallinity in the carbonated zone, associated with the formation of calcium carbonate polymorphs, enhances mechanical properties, while stronger Si-O-(Si, Al, K) bonds improve the network connectivity of the geopolymer (Hajiabadi et al., 2025; Hajiabadi et al., 2023). Thermal shock tests on the geopolymer sealant also showed only a minor decrease in compressive strength, particularly when brine was used as the containment fluid (Hajiabadi et al., 2024). Overall, these findings support the suitability of this sealant for the downhole application.

With the advancement of computational tools, numerical simulations have also become an alternative path to understand the chemical and physical properties of this material and microstructural changes due to its exposure to CO_2 under well conditions. Most existing numerical models for reactive transport operate at the macroscale and are primarily focused on capturing bulk phenomena such as leakage pathways, cracking, and material degradation (Xu et al., 2011; Gherardi et al., 2012; Jacquemet and des S, 2025). Xu et al. introduced TOUGHREACT, a simulation model for multiphase reactive geochemical transport in saturated geologic media (Xu et al., 2006). This program can be applied to many geologic systems and environmental problems, including geothermal systems, diagenetic, and weathering processes in homogeneous and heterogeneous porous media (Xu et al., 2006). However, this model is used at the macro to *meso* scale; as a result, this simulation framework needs inputs such as porosity, permeability, and tortuosity (Xu et al., 2006; Xu et al., 2011). These inputs are either estimated by conducting a dedicated experiment or from an empirical relation, which also has limited applicability. Similarly, there are other continuum scale modeling frameworks such as CrunchFlow, HYTEC, and OpenGeoSys, which also simulate the reaction and transport; however, these also require pore structure and microstructure characteristics as input (Steefel et al., 2015; van der Lee et al., 2003; Steefel and Yabusaki, 2000). These models, while invaluable for understanding large-scale behaviours, do not account for the intricate pore-scale interactions that govern such macroscopic performance. Raoof et al. proposed a pore-scale reaction transport model by generating the pore network of the OPC-based sealants by the Complex Pore Network Model and simulated the carbonation of the OPC under CO_2 storage conditions (Raoof et al., 2012). However, Raoof et al. assumed Portlandite as the only reactive phase in the system. Notably, most of the available models have only been applied to OPC-based concrete and have not been developed and/or applied to alkali-activated materials (Marty et al., 2009). Additionally, a few models have been developed that incorporate ion transport, dissolution-precipitation reactions, and microstructural reorganization, especially for the geopolymer-based sealants exposed to GCS well conditions.

To bridge this gap, the objective of the present study is to develop a novel numerical modeling framework, ReacSan, to simulate physical and chemical changes in this newly developed rock-based geopolymer exposed to underground well conditions. ReacSan uses 3D microstructural input to estimate CO_2 dissolution into pore solution under elevated temperature and pressure using a thermodynamics framework. Ion transport within the microstructure is simulated using the Lattice Boltzmann Method (LBM). Lastly, the model was coupled with a thermodynamic model (GEMS) to model the precipitation of the different reaction products. Complementary experiments were conducted by exposing the sealant material to supercritical CO_2 and measuring the depth of carbonation at different times, which was also used to compare the modeling results. Microstructural characterization using a scanning electron microscope (SEM) was also performed to study the microstructure of the CO_2-exposed geopolymer, and compare it with the model outputs.

The structure of this article is as follows: Section 2 presents the description of different modules and formulations used in the numerical model. Section 3 outlines the materials and experimental methods, and Section 4 discusses the simulation results and their comparison with experimental findings.

2. Numerical simulation model

Fig. 1 illustrates the overall flowchart for the reaction transport simulation framework ReacSan. The ReacSan model primarily consists of five components: 1) Input microstructure and hydration products, 2) CO_2 dissolution, 3) Gel dissolution, 4) Ion transport, and 5) Precipitation of reaction products. In the first module, the input microstructure, which contains the 3D distribution of different phases (unreacted raw materials and hydration products), is taken as input. This 3D microstructure of the hydrated one-part geopolymer was generated using Geomicro3D (Gupta et al., 2025). Next, the dissolution of CO_2 and of the binding gel in the pore solution is modeled in modules 2 and 3. Following the dissolution step, the ions transport module is utilized to diffuse the ions in the microstructure of the paste (module 4). Lastly, the precipitation and growth of different reaction products in the microstructure of the paste are modeled in module 5. At that point, the model returns to module 2 and repeats the cycle until the target simulation time is reached. An elaborate description of the five different modules is given in the following sections.

2.1. Initial simulation input

The starting point for the ReacSan framework is a 3D microstructure of the paste. This input microstructure should capture the spatial distribution of key phases, including hydration products, pores, and unreacted particles, along with the pore connectivity. For this work, the input microstructure is derived from GeoMicro3D, a hydration and microstructure modeling platform for alkali-activated materials (Gupta et al., 2025; Chen, 2024; Zuo and Ye, 2021). GeoMicro3D has previously demonstrated its capability to successfully simulate the reaction kinetics and microstructural evolution of one-part geopolymer systems (Gupta

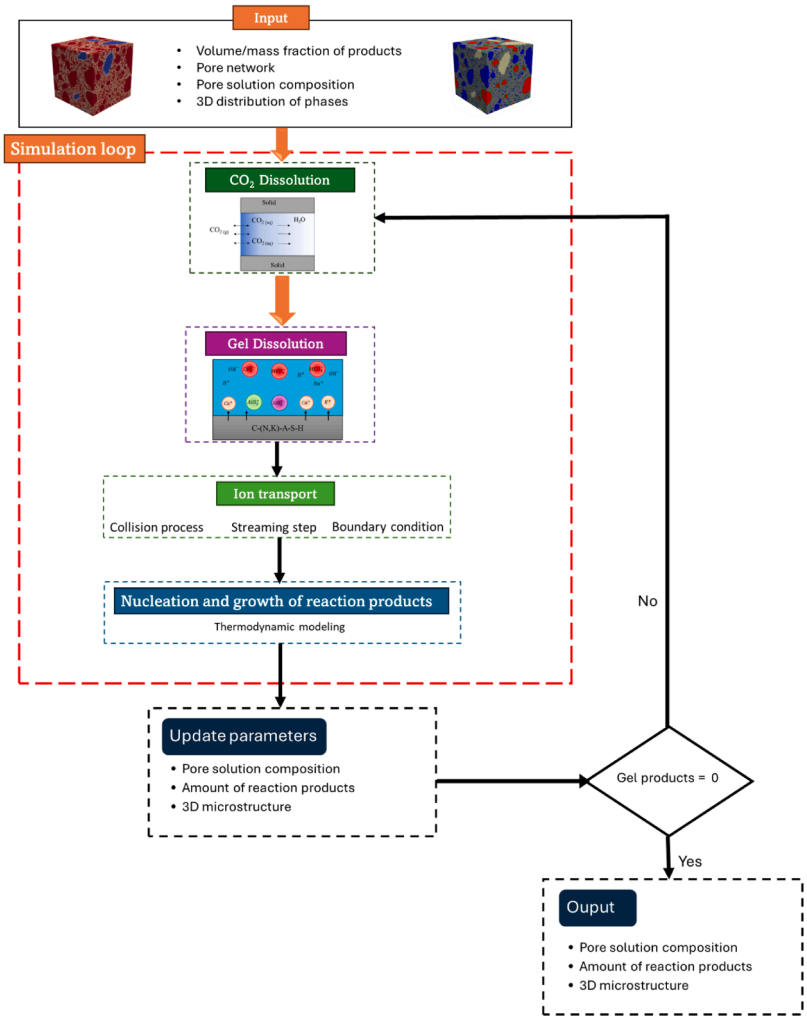

Fig. 1. The overall flowchart of the ReacSan modeling framework.

et al., 2025). In this context, GeoMicro3D models the dissolution of various precursors and the activator by incorporating experimentally determined dissolution rates (Gupta et al., 2025; Zuo and Ye, 2021). This dissolution process is coupled with ion transport and nucleation models to thermodynamically predict both the quantity and type of reaction products, as well as their spatial distribution within the three-dimensional domain. The microstructure and associated chemical data produced by GeoMicro3D have been validated against experimental observations. The input contains volume fractions of different reaction products, which include C-(N, K)-A-S-H gel, hydrotalcite-like phases MA-OH-LDH, zeolites such as natrolite and NAT(K), unreacted raw materials, mainly slag, micro-silica, and granite (Gupta et al., 2025). The pore solution contains the equilibrium concentration of Ca, Al, Si, K, Na, and Mg obtained from the GeoMicro3D. The pictorial representation of the input is shown in Fig. 2. The entire simulation domain size is 150 μm, with a resolution of 1 μm for each voxel.

Notably, the simulation input for the reaction transport framework can also be taken from any other existing numerical simulation platform, such as HYMOSTRUC, μic, or CEMHYD3D, or from X-ray computed tomography (XCT) scanning (Ye, 2003; Van Breugel, 1993; Bentz, 1997; Gupta et al., 2022).

2.2. CO_2 dissolution

In order to calculate the solubility of CO_2 in the pore solution of cement paste at high temperature and pressure, an approach proposed by Choi and Nesic is used (Spycher et al., 2003; Redlich and Kwong, 1949; Choi and Nešić, 2011). This thermodynamic model equates the chemical potential of H_2O and CO_2 using the Redlich–Kwong (RK) equation of state (EOS) (Redlich and Kwong, 1949). At the equilibrium condition, the activity (a_i) of the components (i) in the liquid phase, would be equal to fugacity (f_i) of the gas components (i). This equilibrium relation is defined by true equilibrium constants (K_i) for the component (i) as given below:

$$K_{H_2O} = \frac{f_{H_2O\ (g)}}{a_{H_2O\ (l)}} \tag{1}$$

$$K_{CO_2} = \frac{f_{CO_2\ (g)}}{a_{CO_2\ (l)}} \tag{2}$$

The fugacity (f_i) can be written in terms of pressure (P), fugacity coefficient ($\varnothing_i$) and mole fraction (y_i of component i in gas) as:

$$f_i = \varnothing_i y_i P \tag{3}$$

The equilibrium constants are dependent on temperature (T) and pressure (P) and can be written as:

$$K_{(T,P)} = K^0_{(T,P^0)} \exp\left(\frac{(P - P^0)\bar{V}_i}{RT}\right) \tag{4}$$

Where P^0, R and $\bar{V}_i$ are the reference pressure (1 bar), gas constant, and

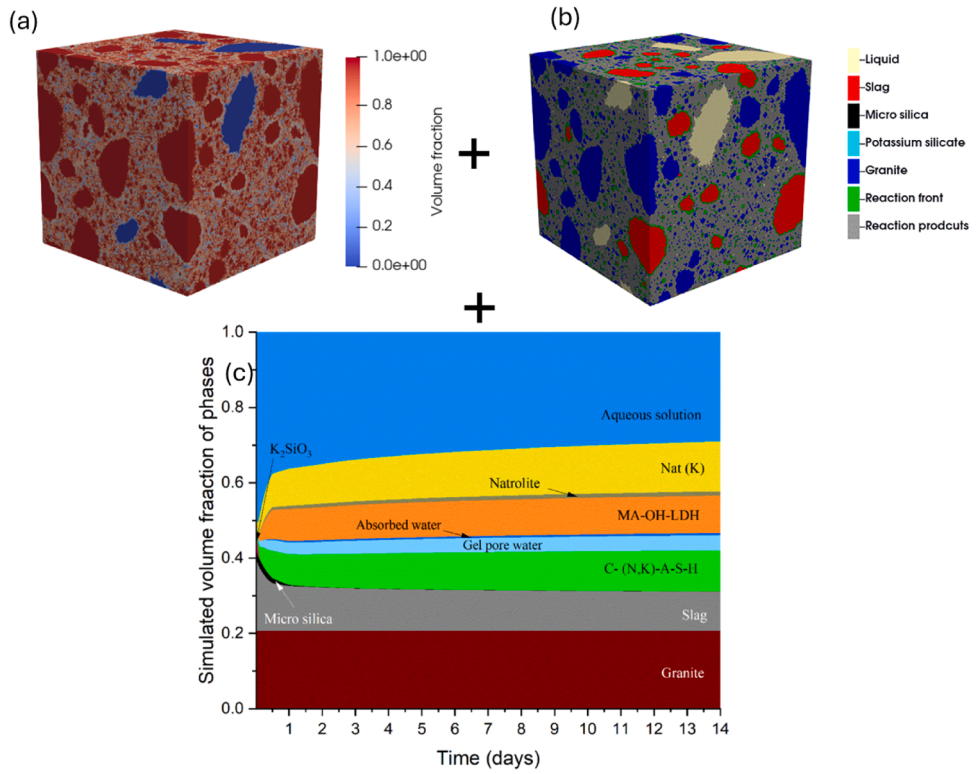

Fig. 2. Inputs required for the ReacSan (a) microstructure of the paste, (b) deposition of the different phases (c) volume fraction of phases and pore solution composition.

average partial molar volume of the pure component i over the pressure interval P^0 to P, respectively. Combining Eq. (4), Eq. (3) and Eq. (1), y_{H_2O} (mol fraction of H_2O in gaseous phase) can be written as:

$$y_{H_2O} = \frac{K^0_{H_2O}.a_{H_2O}}{\varnothing_{H_2O}P}\exp\left(\frac{(P-P^0)\bar{V}_{H_2O}}{RT}\right) \tag{5}$$

Considering Raoults law, the water activity can be approximated by its mole fraction in the water phase ($x_{H_2O} = 1 - x_{CO_2}$). Accordingly, Eq. (5) can be rewritten as:

$$y_{H_2O} = \frac{K^0_{H_2O}.(1-x_{CO_2})}{\varnothing_{H_2O}P}\exp\left(\frac{(P-P^0)\bar{V}_{H_2O}}{RT}\right) \tag{6}$$

Similarly, combining the equations for CO_2, by considering the $a_{CO_2} = 55.50x_{CO_2}$ (Choi and Nešić, 2011), the mole fraction of CO_2 in liquid phase can be written as:

$$x_{CO_2} = \frac{\varnothing_{CO_2}\left(1-y_{H_2O}\right)P}{55.50.K^0_{CO_2}}\exp\left(\frac{(P-P^0)\bar{V}_{CO_2}}{RT}\right) \tag{7}$$

$K^0_{CO_2}$ and $K^0_{H_2O}$ are functions of temperature, and their expression can be found in (Choi and Nešić, 2011). The fugacity coefficients ($\varnothing_{CO_2}$ and $\varnothing_{H_2O}$) is calculated using the volume of the compressed gas phase (V) using the equation given below:

$$\ln(\varnothing_m) = \ln\left(\frac{V}{V-b_{mix}}\right) + \left(\frac{b_k}{V-b_{mix}}\right) - \left(\frac{2\sum_{i=1}^{n}y_i a_{im}}{RT^{1.5}b_{mix}}\right)\ln\left(\frac{V+b_{mix}}{V}\right) + \frac{b_m a_{mix}}{RT^{1.5}b^2_{mix}}\left[\ln\left(\frac{V+b_{mix}}{V}\right) - \frac{b_{mix}}{V+b_{mix}}\right] - \ln\left(\frac{PV}{RT}\right) \tag{8}$$

Here a and b represent the intermolecular attraction and repulsion factor respectively. a_{mix} and b_{mix} are mixture constants for CO_2 and water mixtures. The calculation a_{mix} and b_{mix} and values of a and b can be found in (Choi and Nešić, 2011). The volume of the compressed gas phase (V) is estimated using the Redlich–Kwong (RK) EOS as given below:

$$P = \frac{RT}{V-b} - \left(\frac{a}{T^{0.5}V(V+b)}\right) \tag{9}$$

Solving the above equations allow estimation of the CO_2 mole fraction in the pore solution under different temperature and pressure conditions, as shown in Fig. 3.

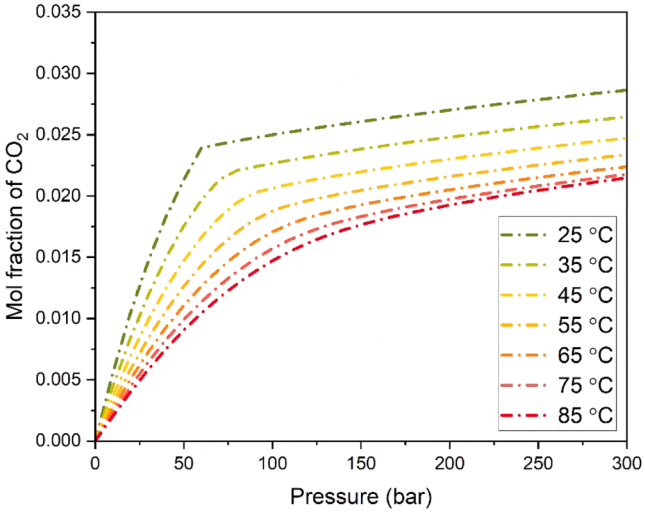

Fig. 3. Solubility of CO_2 in pore solution estimated at different temperatures and pressures.

2.3. Gel dissolution

As a result of increasing carbonate ion concentration in the pore solution, Ca and Mg carbonates start to precipitate, which reduces the Ca and Mg ion concentrations in the pore solution. This disturbs the chemical equilibrium between reaction products and pore solution, leading to dissolution of certain phases and the decalcification of C-(N, K)-A-S-H gel. The dissolution kinetics of these different reaction products are modelled using the Transition state theory (Löher et al., 2025; Lasaga, 1981). According to this theory, the dissolution rate (r_χ) of any phase χ can be written as:

$$r_\chi = r_\chi^+ \left(1 - \left(\frac{IAP_\chi}{Ksp_\chi}\right)^{1/\sigma}\right) \tag{10}$$

- r_χ: Overall dissolution rate (mol/m^{2}s).
- r_χ^+: Forward dissolution rate (far from equilibrium dissolution rate (mol/m^{2}s)).
- IAP_χ: Ion activity product for the phase χ
- Ksp_χ: Solubility product of the phase
- σ: Ratio of dissolution rate of the activated complex relative to the overall reaction rate.

The dissolution equation for any phase can be represented by the dissociation of its constituent ions. An example of C-K-A-S-H, MA-OH-LDH and NAT(K) are given below:

$$(CaO)(Na_2O)_{0.34}(Al_2O_3)_{0.15}(SiO_2)_{1.18}(H_2O)_{1.3} \leftrightarrow Ca^{2+} + 1.18SiO_3^{2-} + 0.31AlO_2^- + 0.68Na^+ + 1.3H_2O \tag{11}$$

$$(MgO)_4(Al_2O_3)(H_2O) + 2H_2O \leftrightarrow 4Mg^{2+} + 2AlO_2^- + 6OH^- \tag{12}$$

$$(K_2O)(Al_2O_3)(SiO_2)_3(H_2O)_2 + 6OH^- \leftrightarrow 2K^{2+} + 2AlO_2^- + 3SiO_3^{2-} + H_2O \tag{13}$$

Different researchers have conducted dissolution tests for C-S-H gel with different Ca/Si ratios at different pH levels (De Windt et al., 2008; Trapote-Barreira et al., 2014). Furthermore, some mathematical models have been proposed to estimate the forward dissolution rates (Marty et al., 2015). The forward dissolution rates (r_χ^+) estimated from the literature vary in a range from 1e-9 to 1e-6 (mol/m^{2}s) (De Windt et al., 2008; Trapote-Barreira et al., 2014; Marty et al., 2015). Due to a very fine resolution of the voxels (1 μm), higher time steps will result in numerical instability in the ion transportation model, hence a lower r_χ^+ would require a very high computation steps and thus increase the simulation time. Therefore, in the current work, a relatively higher forward dissolution rate of 1e-6 (mol/m^{2}s) is used for all the reaction products. Notably, in the current study phases present in the granite such as plagioclase or (K-) feldspar which might react with CO_2 at a very slow rate relative to the hydration products are assumed to be unreactive.

2.4. Ion transport model

Following the gel dissolution step, the ion transport module is used to simulate the transport of different ionic species in the microstructure. As cementitious seals in underground wells are typically under saturated conditions, only diffusive transport is considered. In this study, the Lattice Boltzmann method (LBM) with a cubic lattice with D3Q7 configuration is used. A multi-relaxation time (MRT) approach, which allows distribution functions in different directions to evolve at different relaxation rates, is used in this study (Li et al., 2013; Yoshida and Nagaoka, 2010; Chai et al., 2016). The distribution functions for ion i by LBM-MRT can be written as:

$$g_i(x + c_i\delta t, t + \delta t) = g_i(x,t) - \left(M^{-1}S_dM\right)_{ij}\left[g_j(x,t) - g_j^{eq}(x,t)\right] + \delta t\left[M^{-1}\left(I - \frac{S_d}{2}\right)M\right]_{ij} S_j \tag{14}$$

Where i and j are the diffusion directions $\forall i, j \in [0,6]$. c_i denotes the discrete velocity at x and time t, and can be written as $\delta x/\delta t$, where δx and δt represent the lattice spacing and time. $g_j^{eq}(x,t)$ denotes the equilibrium distribution function, which can be written as:

$$g_j^{eq}(x,t) = \omega_i C \tag{15}$$

where ω_i is the weight coefficient ($\omega_i = \frac{1}{7}\forall i \in [0,6]$), and C is the concentration of ions at any lattice node. I, M and S_d represent the identity matrix, transformation matrix, and diagonal relaxation matrix, respectively, which are given in Eq. (15) and (16).

$$M = \begin{bmatrix} 1 & 1 & 1 & 1 & 1 & 1 & 1 \\ 0 & 1 & -1 & 0 & 0 & 0 & 0 \\ 0 & 0 & 0 & 1 & -1 & 0 & 0 \\ 0 & 0 & 0 & 0 & 0 & 1 & -1 \\ 6 & -1 & -1 & -1 & -1 & -1 & -1 \\ 0 & 2 & 2 & -1 & -1 & -1 & -1 \\ 0 & 0 & 0 & 1 & 1 & -1 & -1 \end{bmatrix} \tag{16}$$

$$S_d = \begin{bmatrix} s_0 & 0 & 0 & 0 & 0 & 0 & 0 \\ 0 & s_1 & 0 & 0 & 0 & 0 & 0 \\ 0 & 0 & s_1 & 0 & 0 & 0 & 0 \\ 0 & 0 & 0 & s_1 & 0 & 0 & 0 \\ 0 & 0 & 0 & 0 & s_2 & 0 & 0 \\ 0 & 0 & 0 & 0 & 0 & s_2 & 0 \\ 0 & 0 & 0 & 0 & 0 & 0 & s_2 \end{bmatrix} \tag{17}$$

Where s_i is the relaxation parameter for the i^{th} moment of the distribution function, such that $s_0 = 0$, $s_1 = 1/\tau$, and $s_2 = 1 - s_1$. τ is the relaxation time, which is related to the diffusion coefficient (D) as:

$$D = \frac{1}{2}\left(\tau - \frac{1}{2}\right)\frac{\delta x^2}{\delta t} \tag{18}$$

S_j in Eq. (14) is the source term in the j^{th} direction, which can be expressed in terms of source term $\overline{S}$ as:

$$S_j = \omega_i \overline{S} \tag{19}$$

The source term takes into account the amount of ions dissolved and consumed in product formation at any step. The concentration of ions at any lattice node can be written as:

$$C(x,t) = \sum_{i=0}^{6} g_i(x,t) \tag{20}$$

The diffusion of SiO_3^{2-}, AlO_2^-, Ca^{2+}, Mg^{2+}, K^+, Na^+, CO_2, CO_3^{2-} and HCO_3^- is considered in the current study, with their diffusion coefficients taken from (Perry, 1950; Zoski, 2006; Huang, 2014; Cussler, 2009) and listed in *Table 1*. The amorphous gel phase (alkali calcium-aluminosilicate hydrate, C-(N, K)-A-S-H gel) is considered diffusive with a relative diffusion coefficient of 0.0025. In contrast, the precursors, the activator, and the secondary crystal reaction products (crystals) are considered non-diffusive. The bounce-back condition is applied to completely non-diffusive lattice nodes. Periodic boundary conditions are implemented for all ions across the top-bottom, and front-back surfaces, ensuring that the ions diffusing out from the top surface re-enter from the bottom surface and vice versa. For ions which were present previously (i.e. SiO_3^{2-}, AlO_2^-, Ca^{2+}, Mg^{2+}, K^+ and Na^+) bounce back condition is applied on the left-right faces. For CO_2 constant concentration boundary condition is applied on the left face, while a zero-flux condition is maintained on the right face using the

Table 1
Diffusion coefficient of different ions.

Ions	SiO_3^{2-}	AlO_2^-	Ca^{2+}	Mg^{2+}	K^+	Na^+	CO_2	HCO_3^-	CO_3^{2-}
D_{ref} (m^2/s)	0.7×10^{-9}	0.6×10^{-9}	0.72×10^{-9}	0.71×10^{-9}	1.96×10^{-9}	1.33×10^{-9}	1.96×10^{-9}	1.1×10^{-9}	0.9×10^{-9}

bounce-back scheme. For CO_3^{2-} and HCO_3^- (which comes from the ion equilibrium with CO_2), a bounce back condition is applied on the left face, while a zero-flux condition is applied on the right face.

2.5. Nucleation and precipitation

The concentration of the different ions in the solution increases due to the dissolution of different phases, and the increase in the carbonate concentration. As a result, the pore solution becomes supersaturated with respect to different reaction products, and these products start to nucleate in the microstructure of the paste. In the current study, the reaction products are mainly divided into two categories, which are carbonates and silica gel. Carbonates are mainly composed of Ca and Mg carbonates, where Ca and Mg derive from the decalcification of the C-(N, K)-A-S-H gel and from hydrotalcite-like phases. The silica gels, which are mainly formed after the decalcification of the C-(N, K)-A-S-H gel, are represented by a number of zeolites. Thermodynamic calculations have been performed using the thermodynamic modeling platform GEMS-selector V3 (Wagner et al., 2012; Kulik et al., 2012). The thermodynamic database used in the model includes the CEMDATA18 database reported in (Lothenbach et al., 2019), and the zeolites21 databases as reported in (Ma and Lothenbach, 2021; Ma and Lothenbach, 2020). The ion activity coefficients in the GEMS- Selector employ the extended Debye-Huckel equation (Wagner et al., 2012; Kulik et al., 2012):

$$log_{10}\left(\gamma_j\right) = \frac{-A_\gamma z_j^2 \sqrt{I}}{1 + \dot{a}B_\gamma \sqrt{I}} + b_\gamma I + log_{10}\left(\frac{x_{jw}}{X_w}\right) \quad (21)$$

Where:

- γ_j- the activity coefficient
- z_j- charge of the ions
- j- the aqueous species
- A_γ, B_γ- the electrostatic parameters
- I- the ionic strength
- x_{jw}- the mole quantity of water
- X_w- the total mole amount of the aqueous phase
- $\dot{a}$- the average ion size
- b_γ- the parameter for common short-range interactions of the charged species

The extended Debye-Hückel expression is applied under the assumption of low to moderate ionic strength of 1–2 molal, with fixed ion-size parameters and without accounting for short-range interactions or complexation effects. The thermodynamic data for different carbonates and zeolites used in this study are given in Table 2 (Ma and Lothenbach, 2021; Ma and Lothenbach, 2020; Ma and Lothenbach, 2020).

3. Materials and experimental methods

3.1. Materials

A one-part geopolymer formulation was developed using a dry-mix method, targeting a low-calcium aluminosilicate matrix (CaO < 10 wt. %). The precursor blend included ground granite (sourced from south-western Norway, 5–150 μm), granulated blast furnace slag (quenched GGBFS), and high-purity amorphous micro-silica. Key physical parameters such as particle size distribution, density, surface area (BET), and bulk composition (via XRF) are summarized in prior work (Hajiabadi et al., 2025).

Activation was achieved using anhydrous potassium silicate (molar modulus ratio ~3.9), with supplementary additions of aluminum hydroxide and potassium hydroxide to optimize the Si/Al ratio and enhance the dissolution rate, respectively. The complete formulation, comprising aluminosilicate precursors, solid activators, and distilled water (water-to-solid ratio of 0.33 by weight), is detailed in (Hajiabadi et al., 2025).

3.2. Exposure to CO_2

Verification of the model presented here was achieved through comparison with experimental studies (van Noort et al., 2025). Van Noort et al. exposed samples of the rock-based geopolymer studied here to wet supercritical CO_2 at pressure and temperature conditions typically expected during geological carbon storage (80 °C and 10 MPa CO2-pressure) (van Noort et al., 2025). These experiments were performed with durations of 4, 8, and 16 weeks (van Noort et al., 2025). Reacted microstructures were studied using SEM (with EDS). To further validate the model, additional tests were performed exposing sample cylinders to wet supercritical CO_2 for shorter durations. In these tests, single, water-saturated cylinders of the cured geopolymer sealant (ø 12 mm, and length 30 mm – from the same sample batch as used in (van Noort et al., 2025)) were placed in a small titanium pot, which was subsequently placed in an externally-heated pressure vessel (internal

Table 2
Thermodynamic properties of phases included as the products for modelling.

Phase	V^0 (cm^3/mol)	$\Delta_f H^0$ (kJ/mol)	$\Delta_f G^0$ (kJ/mol)	S^0 (J/mol.K)	C_p^0 (J/mol.K)
Scolecite ($CaAl_2Si_3O_{10}{\cdot}3H_2O$)	172.42	−6011.6	−5560.52	367	383
Analcime ($Na_2(AlSi_2)_2O_2(H_2O)_2$)	194.8	−6575.8	−6139.70	469	425
Chabazite (Na) ($Na_2(Al_2Si_4)O_{12}.6(H_2O)$)	249.9	−7808.3	−7117.55	548	578
Chabazite (K) ($K_2Al_2Si_4O_{12}.4(H_2O)$)	252.9	−7228.7	6686.63	607	564
Chabazite (Ca) ($Ca(Al_2Si_4)O_{12}.6(H_2O)$)	247.6	−7806.7	−7144.01	581	617
Heulandite (K) ($K_{2.22}Al_{2.22}Si_{6.78}O_{18}.4.7(H_2O)$)	324.8	−10,289.3	−9487.07	586	665
Heulandite (Ca) ($Ca_{1.07}Al_{2.14}Si_{6.86}O_{18}.4.4(H_2O)$)	317.8	−10,118.6	−9353.66	541	611
Stilbite (K) ($K_{2.2}Al_{2.2}Si_{6.8}O_{18}.4.8(H_2O)$)	316.7	−10,301.1	−9505.55	630	669
Stilbite (Ca) ($Ca_{1.11}Al_{2.22}Si_{6.78}O_{18}.6.8(H_2O)$)	327.4	−10,815.6	−9944.75	748	782
Calcite ($CaCO_3$)	36.9	−1207	−1129	92.7	81.9
Huntite ($CaMg_3(CO_3)_4$)	123	−4533	−4206	300	310
Artinite ($Mg_2(OH)_2(CO_3)(H_2O)_3$)	96.2	−2921	−2568	233	248
Hydromagnesite ($Mg_5(OH)_2(CO_3)_4(H_2O)_4$)	208.8	−6514.9	−5864.2	503.7	526.6
Nesquehonite ($MgCO_3(H_2O)_3$)	74.8	−1977.3	−1723.7	195.6	237.8
Magnesite (MgCO3)	28.0	−1113	−1029.5	65.7	75.8

volume 100 ml). A small quantity of demineralized water was then added to the vessel (without direct contact with the sample), and the vessel was sealed with a Teflon O-ring. Then, the vessel was pressurized with CO_2, and heated through an external heating sleeve controlled by a thermocouple placed inside the vessel, near the sample, to 80 °C and 8–10 MPa. Once the sample had been exposed for the intended duration, the heating was switched off to allow the sample to cool. The remaining pressure was then carefully released to prevent sample damage, and the sample was retrieved. During one test, a pressure loss was observed approximately 1.5 h after the start of the experiment, and the pressure gradually decreased. Further heating was discontinued, and the sample was exposed to elevated temperatures for approximately 3.5 h; temperature and pressure profiles were measured. The retrieved samples were wrapped tightly in parafilm and then sealed in a ziplock bag until the phenolphthalein test was performed.

The carbonation depth of cement paste samples was determined using the phenolphthalein indicator test. Following exposure, the samples were split, and phenolphthalein solution (1 % in ethanol) was sprayed on the freshly fractured surface. The uncarbonated regions turned pink, while the carbonated areas remained colorless

3.3. SEM analysis

Microstructural imaging and elemental mapping were conducted using scanning electron microscopy (SEM) on two advanced instruments: the Zeiss Supra 35VP and the JEOL JSM-IT800. Both systems were equipped with backscattered electron (BSE) detectors and energy-dispersive X-ray spectroscopy (EDS) for compositional analysis.

Cross-sectional samples were taken from two depths: the upper region, fully exposed to reactive fluid, and the central region, primarily affected by radial diffusion. One disc from each location was designated for SEM-EDS analysis.

Prior to imaging, samples were dried at 40 °C and stored under vacuum for 24 h to minimize moisture-related artifacts. Due to the small specimen size, the analysis was limited to comparing the upper and central sections rather than isolating finer chemical gradients or reaction zones.

4. Results and discussion

This section will discuss the results from the numerical simulation, experiments, and their comparison.

4.1. Modeling observations

Fig. 4 plots the pH and relative concentrations of different carbonate species in the pore solution at an intermediate stage of carbonation. It is apparent from Fig. 4(a) that the pH of the pore solution dropped drastically up to the carbonation depth with the penetration of CO_2 through the microstructure. As the CO_2 dissolves in the pore solution, it dissociates into HCO_3^- and CO_3^{2-} and the concentrations of these individual species is dependent on the pH of the solution. From Fig. 4(a), it can be seen that the pore solution has majorly three ranges of pH, viz, low pH, medium pH, and high pH. Fig. 4(c–e) plot the relative concentrations of different carbonate species, showing that H_2CO_3 is the main species of CO_2 in the low pH zone, while HCO_3^- dominates in the medium pH zone, and CO_3^{2-} dominates in the high pH zone. Fig. 4(b) plots a qualitative variation of the concentration of different carbonate species with pH. The equilibrium constant for the dissociation of the H_2CO_3 (given in Eq. (22)) is approximately 4.3×10^{-7} which makes HCO_3^- the dominant species in slightly acidic to neutral solutions (pH ~6–9). The second dissociation (given in the Eq. (23)) has an equilibrium constant of 4.8×10^{-11} which predominates only in alkaline solutions (pH > 9). Hence, the current numerical modeling can capture the drop of pH as well transition of different carbonate species with pH (Raoof et al., 2012).

$$H_2CO_3 \rightleftharpoons H^+ + HCO_3^- \tag{22}$$

$$HCO_3^- = H^+ + CO_3^{2-} \tag{23}$$

Fig. 5(a) plots the phase assemblage of the one-part geopolymer due to carbonation as obtained from the numerical simulation. Due to a drop in the pH, the original hydration products (C,(N, K)-A-S-H, MA-OH-LDH, natrolite, and NAT(K)) start to disintegrate and dissolve into the pore solution, and then react with carbonate ions to precipitate carbonates and silica gels (outlined in Table 2). For the current material, the C-(N, K)-A-S-H gel is mainly composed of INFCK

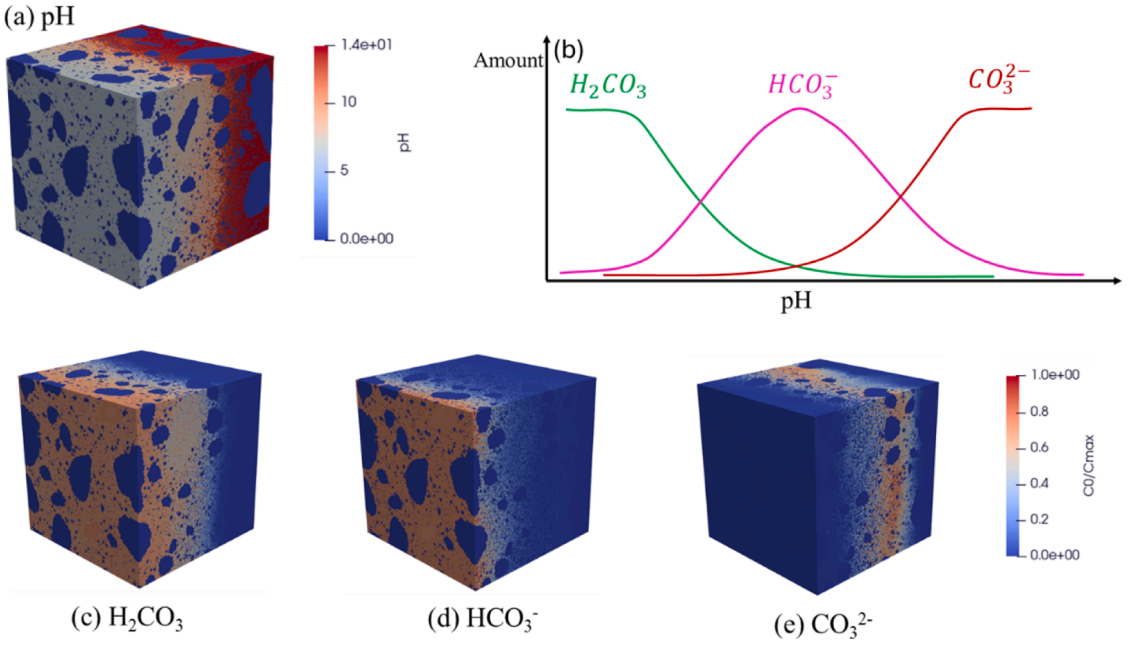

Fig. 4. (a) pH of the pore solution obtained from the model, (b) qualitative variation in concentration of carbonate species with pH, (c) relative concentration of H_2CO_3 in the pore solution, (d) relative concentration of HCO_3^- in the pore solution, (e) relative concentration of CO_3^{2-} in the pore solution.

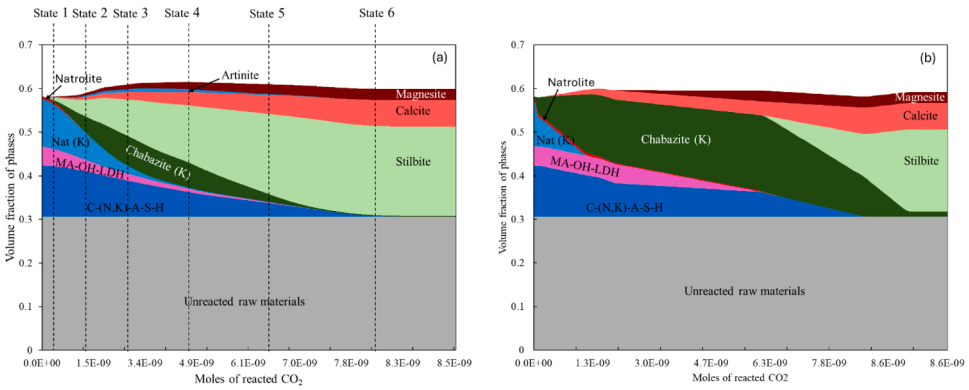

Fig. 5. (a) Simulated volume proportion of phases with ReacSan (b) volume fraction of phases using GEMS.

$((CaO)_1(K_2O)_{0.3125}(SiO_2)_{1.5}(H_2O)_{1.1875})$ and INFCKA $((CaO)(K_2O)_{0.34375}(Al_2O_3)_{0.15625}(SiO_2)_{1.1875}(H_2O)_{1.3})$ (Gupta et al., 2025). As the CO_2 penetrates through the microstructure of the paste, first the MA-OH-LDH and natrolite, and NAT(K) start to react and transform to carbonates and other silica gel. This is in much agreement with the literature, as Ke et al. (Ke et al., 2020) and Farnaz et al. (Aghabeyk et al., 2024) conducted a thermodynamic study about the phase changes due to carbonation and observed that hydrotalcite-like phases convert to carbonated hydrotalcite and ultimately convert to magnesium carbonate and silica gels. Further, the decalcification of the C- (N, K)-A-S-H gels takes place, leading to the formation of calcium carbonates. It can be seen from Fig. 5(a) that initially, chabazite (K) is the main silica gel formed (with a Si/Al ratio of 2), which then further converts to stilbite (with a Si/Al ratio of approx. 3) as carbonation continues. The initial precipitation of low-Si/Al chabazite is driven by the release of Al ions from the dissolution of Nat(K), natrolite, and MA-OH-LDH. The dissolution of these species maintains a sufficient concentration of Al to form Chabazite. However, with further progression of the carbonation and dissociation of the INFCK $((CaO)(K_2O)_{0.3125}(SiO_2)_{1.5}(H_2O)_{1.1875})$ from the C- (N, K)-A-S-H, more Ca, Si and K ions are released into the pore solution. This increases the Si ion concentrations in the pore solution, resulting in the conversion of chabazite (K) into higher-Si/Al stilbite (K). At the same time, Ca and Mg are released from the gel precipitates as $CaCO_3$ and $MgCO_3$ in the pores. In previous studies involving identical one-part geopolymer compositions subjected to dynamic exposure to CO_2-saturated water (via coreflooding), calcite precipitation was observed, and magnesite precipitation was found at the outlet end of the specimens (Hajiabadi et al., 2025). This was attributed to the leaching and downstream migration of Mg^{2+} ions from interior regions (refer to SEM micrographs Fig. A1 in Appendix A1). Additionally, the formation of chabazite-K was also observed in those experiments, likely resulting from interaction with tap water containing dissolved carbonate ion species (Hajiabadi et al., 2025). This secondary zeolite phase was also predicted by the model and is consistent with known geopolymer–water interaction. It is also apparent from Fig. 5(a) that the total solid volume has increased after complete carbonation of the phases, which (under conditions of constant overall volume) implies a decrease in the overall porosity of the material. The porosity of the paste before exposure to the CO_2 was 0.42, while after complete carbonation of the paste, the porosity of the sample reached 0.40. It is important to note that this represents the total porosity of the paste samples, which is obtained by subtracting the total solid volume from the total volume. Hence, this porosity also includes the fraction of the volume occupied by the gel and absorbed water in the C- (N, K)-A-S-H and silica gel.

Fig. 5(b) plots the phase assemblage due to carbonation, performed using GEMS separately. This simulation was performed by using moles of the different hydration products as input and stepwise addition of CO_2. A comparison of the two figures reveals that the phase transitions predicted by the current modeling framework closely align with the GEMS results. The differences observed can be attributed to the incorporation of ion transport and the rate-dependent dissociation of various phases in the current model, providing a more accurate representation of the underlying processes.

In order to understand and visualize the spatial distribution of different carbonation products, such as carbonates and silica gels, the microstructure is analyzed at different stages of carbonation as denoted by the vertical lines in Fig. 5(a). Six stages in Fig. 5(a) are denoted as states 1, 2, 3, 4, 5, and 6. Fig. 6(a–d) plot the volume fraction of the chabazite (K), stilbite (K), $CaCO_3$, and $MgCO_3$, respectively, in the direction of the carbonation. Focusing on Fig. 6(a), it can be observed that the peak of chabazite (K) keeps moving backwards with an increase in the extent of carbonation, and ultimately, the peak vanishes at state 6. On the other hand, the peaks for the stilbite (K) (from Fig. 6(b)) keep accumulating at the CO_2 exposure surface, and then into the progressively carbonated microstructure. These different temporal distribution patterns for these two low-calcium gels are explained by the initial formation of chabazite (K), followed by its gradual conversion into stilbite (K) with increasing carbonation. From Fig. 6(c) and Fig. 6(d), it is evident that the precipitation of carbonate phases ($CaCO_3$ and $MgCO_3$) is significantly higher near the exposure surface compared to the deeper regions. This is because, as carbonate phases begin to precipitate at the exposure surface, a concentration gradient for Ca^{2+} and Mg^{2+} ions is established, which drives the diffusion of these ions from the inner regions toward the exposed face, leading to increased precipitation of $CaCO_3$ and $MgCO_3$ there. This mechanism explains the localized accumulation of carbonate phases at the carbonation front, which was also observed on samples exposed to GCS conditions in (van Noort et al., 2025). In their study, Van Noort et al. reported a somewhat elevated Ca/Si-ratio near the surface of geopolymer samples batch-exposed to wet supercritical CO_2, based on SEM-EDS analyses, as well as elevated density close to the sample surface, based on CT-scanning. Notably the scale of SEM-EDS analyses by Van Noort et al. and the current simulation is different.

Fig. 7 illustrates the 3d microstructure generated from the current numerical framework before and after exposure to CO_2. The arrow shown below each microstructure shows the direction of flow of CO_2. Fig. 7(a–c) show the volume fraction of all phases (including raw materials, hydration products and reaction products) before and after CO_2 exposure at state 3 and state 6, respectively. It is evident that reaction products such as carbonated and silica gel are precipitating in the available pore spaces as the carbonation is proceeding. By comparing Fig. 7(a) and (c) it is apparent that the reaction products are more distributed as compared to unexposed microstructure. Fig. 7(d–f) shows the volume fraction distribution of the hydration products, carbonates and silica gel in the microstructure at state 3. It can be seen that CO_2 has penetrated up to a certain depth, where the hydration products have dissolved (shown in Fig. 7(d)). In the same carbonated zone, the precipitation of the carbonates and silica can be observed, while not much

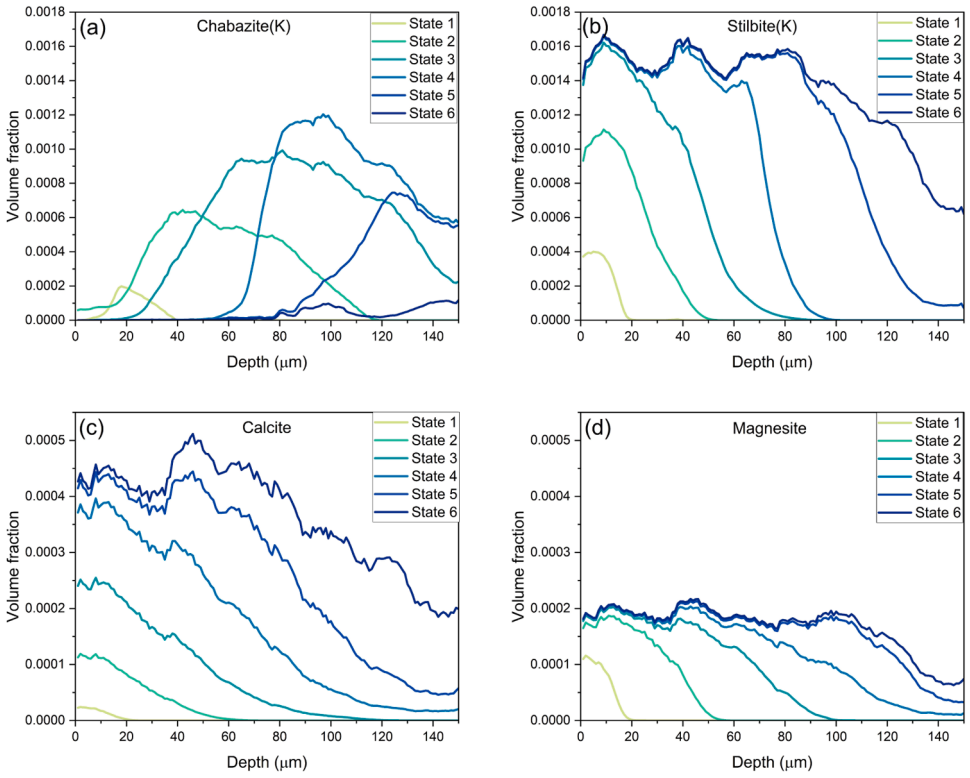

Fig. 6. Precipitation of different products along the depth of carbonation (a) chabazite (K), (b) stilbite (K), (c) calcite and (d) magnesite.

precipitation have started in the uncarbonated zone (shown in Fig. 7 (e–i) shows the volume fraction distribution of the hydration products, carbonates and silica gel at state 6. At this state the CO_2 has penetrated in the entire microstructure, which is evident by the complete dissolution of the hydration products in Fig. 7(h). It can also be observed that the carbonate phases precipitate in the available pore spaces and fill the porosity, while the low calcium phases deposit more homogenously throughout the microstructure. These observations are very similar to the SEM images observed for alkali activated slag exposed to supercritical CO_2 by Samarakoon et al. (2022). SEM images were also conducted in this study and are discussed in the next section.

4.2. SEM observations

SEM analysis was performed on the top (the exposure-facing) and the middle sections of geopolymer specimens following exposure to CO_2-rich conditions to assess spatial variation in carbonation effects. Fig. 8(a) and (b) present SEM micrographs of the top surfaces. Distinct rhombohedral calcite crystals are prominently observed, occupying and partially occluding the pore spaces within the geopolymer matrix. This secondary mineralization contributes to a reduction in porosity, and a potential enhancement of the sealing capacity of the material. These observations are in agreement with predictions from the reactive transport simulations, which also indicate calcite precipitation in this region (see Figs. 6 and Fig. 7(c)).

Fig. 8(c) and (d) present SEM micrographs obtained from the middle sections of the specimens. In contrast to the top region, this area exhibits much lower calcite precipitation. EDS mapping confirms the presence of finely dispersed calcium carbonate phases with morphologies characteristic of vaterite (shown in Fig. 8d). The coexistence of both calcite, the thermodynamically stable polymorph, and vaterite, a metastable phase, in the interior zones, which were less exposed to the advancing carbonation front than the inlet surface, suggests a kinetically controlled precipitation pathway, where vaterite precipitates first and then gradually transforms into calcite via a dissolution-reprecipitation mechanism. It is important to note that the current numerical model is restricted to equilibrium-based thermodynamic predictions and therefore does not simulate the formation of metastable or kinetically favored phases; consequently, vaterite precipitation was not predicted in the simulation results.

4.3. Carbonation depth data comparison

In order to estimate the depth of the carbonation, a finite volume mesh was generated (at the macro scale) with dimensions of 12 mm in length and a cross-sectional area of 0.1 × 0.1 mm. The mesh resolution was set to 10 μm to balance accuracy with computational efficiency. The small cross-section minimized the number of elements, thereby reducing computation time while maintaining the representativeness of the microstructure.

Each element of the mesh was initialized with the pore solution composition derived from GeoMicro3D simulations. The diffusion coefficient for individual elements was calculated based on the effective diffusion coefficient of the cube at the microscale, incorporating the 3D spatial distribution of reaction products and unreacted phases. These spatial distributions, obtained from GeoMicro3D, account for the heterogeneity in the microstructure and enable an accurate representation of ion transport during carbonation. The effective diffusivity of the microstructure is obtained by solving the ion transport through the microstructure of the paste, where individual nodes have diffusivity based on the volume fraction of the reaction products (Gupta et al., 2025; Zuo and Ye, 2021). The Dirichlet boundary condition is applied at the inlet and outlet ends of the cube with concentrations of C_i=2 M and C_o=1 M, respectively. Periodic boundary conditions were applied on the other faces. The simulation was performed using LBM MRT as discussed in Section 2.4, until the relative change in the average concentration reached <1e-6. The effective diffusion is calculated by estimating the volume average of the steady stage flux ($\vec{J}$) across the heterogeneous media using the equation given below:

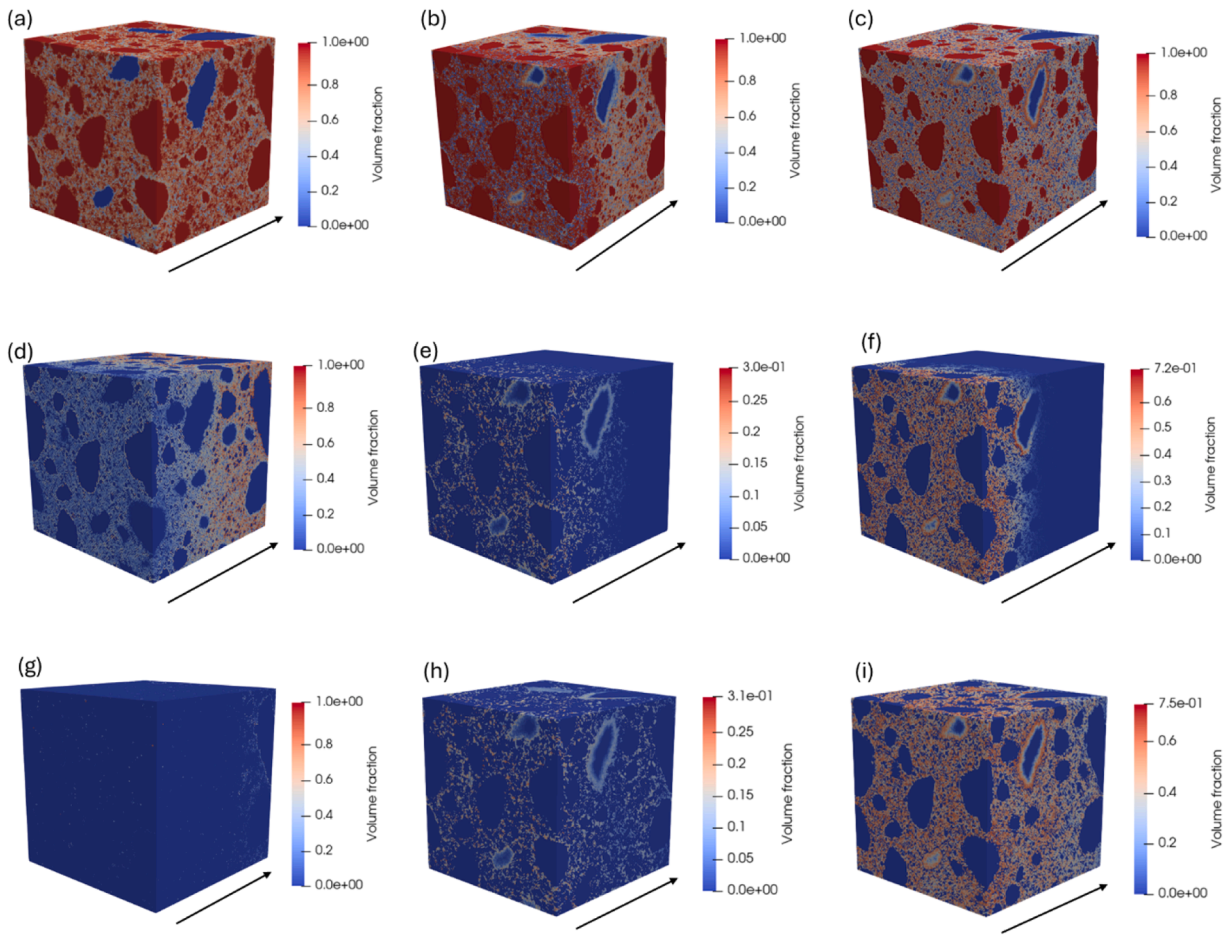

Fig. 7. Microstructural evolution and product distribution: (a) initial paste microstructure, (b, c) microstructure after states 3 and 6, respectively, (d, g) hydration products at states 3 and 6, respectively, (e, h) carbonate precipitation at states 3 and 6, respectively, (f, i) silica gel precipitation at states 3 and 6, respectively.

$$D_{eff} = \frac{\left\langle \hat{n}.\vec{J} \right\rangle}{\langle \hat{n}.\vec{\nabla}C \rangle} \tag{24}$$

Here $\langle m \rangle$ represents the volume average quantity of m, and C is the concentration of the ion. The flux at different nodes is calculated using the equation given below (Xuan et al., 2010):

$$J = \sum_i c_i g_i \left(\frac{\tau - 0.5}{\tau} \right) \tag{25}$$

Here τ, c_i and g_i are the relaxation time, lattice velocity, and distribution functions as described in Section 2.4. After performing the simulation, the relative diffusion coefficient was obtained to be 0.05.

In order to simulate the experimental conditions, Dirichlet boundary conditions were applied at both ends of the finite volume mesh. The dissolved concentration of the CO_2 at the boundary nodes was estimated based on the applied pressure (shown in Fig. 9). The temperatures under both exposure conditions were 80 °C.

Further reaction transport simulation was performed, information about the different ion concentrations at different nodes was transferred to GEMS, and the pH of the pore solution was estimated. Fig. 10 compares the result to two samples exposed for either 3.5 h or 16 h as described in Section 3.2 to the model results. Testing with phenolphthalein showed that after exposure for ~3.5 h (Exposure 1), the depth of the carbonation was nearly 2 mm, while after 16 h, the sample was fully carbonated (Exposure 2). When comparing these experimental results to Fig. 10a, which plots the pH variation across the depth of the sample as estimated from the model, a strong agreement is obtained as the model predicts that for Exposure 1 phenolphthalein would give a pink color at a depth around 2 mm, while for Exposure 2, the pH has dropped below 8.5 indicating complete carbonation of the sample. These observations prove the rationality of the numerical model capturing the progression of carbonation and microstructural changes. Further studies should be conducted to accurately estimate the decalcification rates of different gels and incorporate multi-phase flow, broadening its applicability to different GCS scenarios.

Spontaneous imbibition refers to the capillary-driven displacement of a non-wetting fluid by a wetting fluid in porous media and is commonly encountered in multiphase systems, including certain GCS scenarios. For example, the injection of dry supercritical CO_2 may lead to local desaturation near the injection interface, potentially initiating counter-imbibition as water moves toward the drying zone (Hajiabadi et al., 2021; Chang et al., 2016; Hall, 2019). However, the conditions investigated in this study involved fully water-saturated specimens exposed to wet $ScCO_2$. The absence of a dry gas phase and the static exposure setup preclude the development of spontaneous or reverse imbibition mechanisms. Therefore, such processes are not expected to influence the observed reactive transport behavior or carbonation front evolution in the present system.

While the present study demonstrates the capabilities of the ReacSan framework in simulating reaction–transport processes in a granite-based one-part geopolymer under geological carbon storage (GCS) conditions, several avenues remain for further development. Dedicated experimental studies are essential to quantitatively assess the evolution of microstructural features such as hydration gel content, carbonate polymorphs, silica gel formation, and porosity over time. These measurements would enable improved calibration of the model parameters and

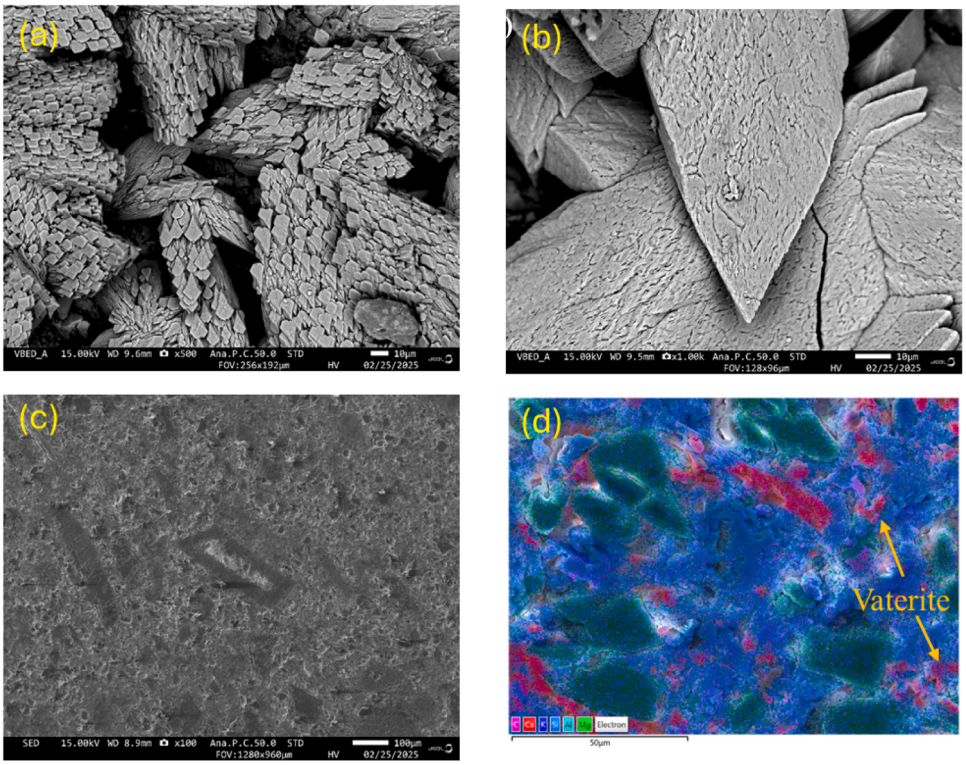

Fig. 8. SEM-EDS images of the one-part geopolymer after exposure to CO_2 (a) and (b) at the inlet of the specimens (c) and (d) from the middle portion of the specimens.

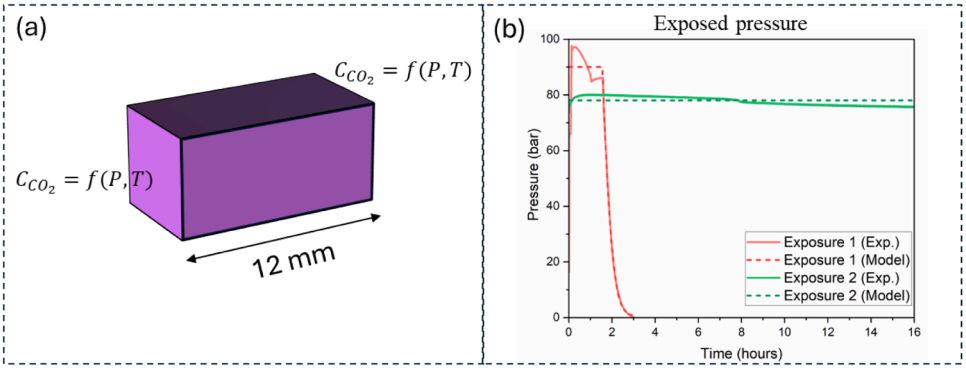

Fig. 9. (a) Pictorial representation of the simulated sample and its boundary conditions (b) exposed and modeled pressure applied to the CO_2 exposed sample.

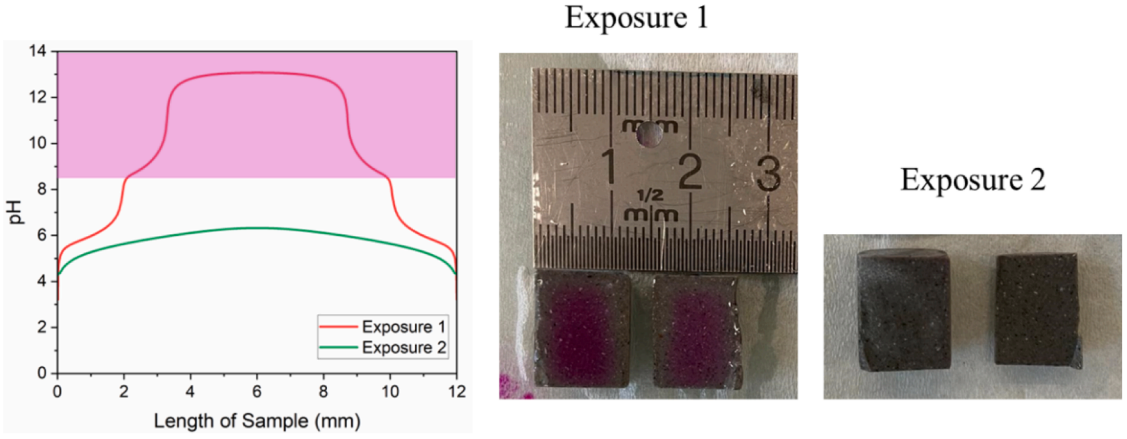

Fig. 10. pH profile obtained from the model for the two exposed conditions and images of the samples from the experiments after the phenolphthalein test.

enhance predictive accuracy. In addition, the synergistic impact of simultaneous exposure to CO_2 and brine—especially relevant for saline aquifers and offshore storage sites—warrants further investigation. Incorporating these conditions into the experimental–numerical framework will offer a more representative understanding of in situ performance. Thermal shocks induced by the injection of supercritical CO_2 present another critical challenge in wellbore environments. Future versions of the ReacSan framework should incorporate a coupled thermo-chemo-mechanical model to capture such interactions and their effects on microstructural degradation (Gupta et al., 2023; Gupta et al., 2023). This may also be extended to simulate cracking and its feedback on transport and reaction kinetics. Finally, the degradation of the steel–concrete interface remains a key vulnerability in GCS systems. Ongoing and future work will aim to model chemical attack, corrosion-induced expansion, microcracking, and interfacial debonding at this interface to provide a more holistic picture of sealant durability under real-world conditions.

5. Conclusions

In the current study, a combined experimental and numerical approach was employed to investigate the reaction and transport of CO_2 through the microstructure of a one-part granite-based geopolymer, a material developed for CCS applications. A novel numerical simulation framework, ReacSan, is developed to simulate the reaction and transport of CO_2 through the paste microstructure. ReacSan can simulate microstructure change in the one-part geopolymer due to its exposure to CO_2. The major conclusions from the current study are:

(a) The initial input for this framework is obtained from GeoMicro3D, which provides 3D microstructure of the alkali activated materials, volume fraction of different reaction products and its deposition in the microstructure, ion concentration of the different ions such as Ca, Mg, Si, Al, K and Na in the pore solution.
(b) The dissolution of CO_2 under GCS well conditions (high temperature and pressure) is modelled using the thermodynamic model based on the Redlich–Kwong (RK) equation of state (EOS). Further, the dissolution of gels is modeled using the transition state theory.
(c) The transport of different ions is modeled using the lattice Boltzmann method (LBM), and chemical reactions and precipitation of various products are simulated through thermodynamic modeling using GEMS.
(d) SEM analysis revealed the precipitation of calcite at the exposed surface (top). Further into the sample, both vaterite and calcite are observed, indicating the initial precipitation of kinetically favored vaterite and subsequent transformation into thermodynamically stable calcite.
(e) Based on phenolphthalein testing on experimentally exposed samples, carbonation (as indicated by a decrease in sample pH) penetrates rapidly (within a few hours for cylindrical samples with a diameter of 12 mm). The simulated carbonation depth (pH profile) shows good agreement with the experimental results, demonstrating the validity of the model.

CRediT authorship contribution statement

Mayank Gupta: Writing – review & editing, Writing – original draft, Visualization, Validation, Software, Methodology, Formal analysis, Conceptualization. **Seyed Hasan Hajiabadi:** Writing – review & editing, Writing – original draft, Methodology, Investigation. **Farnaz Aghabeyk:** Writing – review & editing, Software. **Yun Chen:** Writing – review & editing, Visualization. **Reinier van Noort:** Writing – review & editing, Writing – original draft, Supervision, Methodology, Funding acquisition. **Mahmoud Khalifeh:** Writing – review & editing, Supervision, Conceptualization. **Guang Ye:** Writing – review & editing, Supervision, Funding acquisition.

Declaration of competing interest

The authors declare that they have no known competing financial interests or personal relationships that could have appeared to influence the work reported in this paper.

Acknowledgments

The CEMENTEGRITY project is funded through the ACT programme (Accelerating CCS Technologies, Horizon2020 Project No 691712). Financial contributions from the Research Council of Norway (RCN), the Netherlands Enterprise Agency (RVO), the Department for Energy Security & Net Zero (DESNZ, UK), and Harbour Energy are gratefully acknowledged.

Appendix

Fig. A1

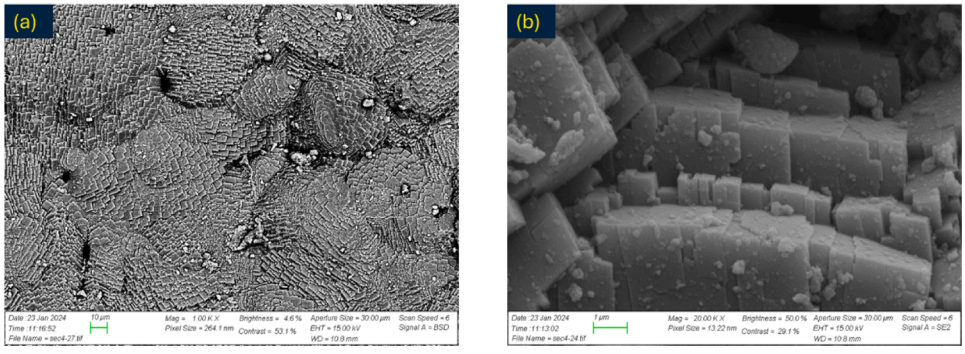

Fig. A1. SEM images of one-part geopolymer exposed to a flow of CO2-saturated water, showing precipitated magnesite.

References

Aghabeyk, F., Chen, B., Gupta, M., Miranda de Lima, L., Chen, Y., Ye, G., 2024. Mix design guidance for alkali-activated pastes incorporating MSWI bottom ash under accelerated carbonation condition: insights from thermodynamic modelling. In: 78th RILEM Annual Week & RILEM International Conference on Sustainable Materials & Structures.

Ahmad, M.R., Chen, B., Shah, S.F.A., 2020. Influence of different admixtures on the mechanical and durability properties of one-part alkali-activated mortars. Constr. Build. Mater. 265, 120320. https://doi.org/10.1016/j.conbuildmat.2020.120320.

Bai, M., Zhang, Z., Fu, X., 2016. A review on well integrity issues for CO 2 geological storage and enhanced gas recovery. Renew. Sustain. Energy Rev. 59, 920–926. https://doi.org/10.1016/j.rser.2016.01.043.

Bakharev, T., 2005. Resistance of geopolymer materials to acid attack. Cem. Concr. Res. 35, 658–670. https://doi.org/10.1016/j.cemconres.2004.06.005.

Barletgouedard, V., Rimmele, G., Porcherie, O., Quisel, N., Desroches, J., 2009. A solution against well cement degradation under CO2 geological storage environment. Int. J. Greenhouse Gas Control 3, 206–216. https://doi.org/10.1016/j.ijggc.2008.07.005.

Bentz, D.P., 1997. Three-dimensional computer simulation of Portland cement hydration and microstructure development. J. Am. Ceram. Soc. 80, 3–21. https://doi.org/10.1111/j.1151-2916.1997.tb02785.x.

Chai, Z., Huang, C., Shi, B., Guo, Z., 2016. A comparative study on the lattice Boltzmann models for predicting effective diffusivity of porous media. Int. J. Heat Mass Transf. 98, 687–696. https://doi.org/10.1016/j.ijheatmasstransfer.2016.03.065.

Chang, C., Zhou, Q., Kneafsey, T.J., Oostrom, M., Wietsma, T.W., Yu, Q., 2016. Pore-scale supercritical CO2 dissolution and mass transfer under imbibition conditions. Adv. Water Resour. 92, 142–158.

Chen, Y., 2024. Thermodynamics, Reaction Kinetics, and Microstructure of Alkali-Activated Fly Ash - An Experimental and Modeling Study. Delft University of Technology.

Choi, Y.-S., Nešić, S., 2011. Determining the corrosive potential of CO2 transport pipeline in high pCO2–water environments. Int. J. Greenhouse Gas Control 5, 788–797. https://doi.org/10.1016/j.ijggc.2010.11.008.

Cussler, E.L., 2009. Diffusion: Mass Transfer in Fluid Systems. Cambridge university press.

De Windt, L., Marsal, F., Tinseau, E., Pellegrini, D., 2008. Reactive transport modeling of geochemical interactions at a concrete/argillite interface. Tournemire site (France), Physics and Chemistry of the Earth 33, S295–S305. https://doi.org/10.1016/j.pce.2008.10.035. Parts A/B/C.

Echevarria Huaman, R.N., Jun, T.X., 2014. Energy related CO2 emissions and the progress on CCS projects: a review. Renew. Sustain. Energy Rev. 31, 368–385. https://doi.org/10.1016/j.rser.2013.12.002.

Eid, E., Tranggono, H., Khalifeh, M., Salehi, S., Saasen, A., 2021. Impact of drilling fluid contamination on performance of rock-based geopolymers. SPE J. 26, 3626–3633.

Field, C.B., Barros, V.R., 2014. Climate Change 2014–impacts, Adaptation and Vulnerability: Global and Sectoral Aspects. Cambridge University Press.

Gherardi, F., Audigane, P., Gaucher, E.C., 2012. Predicting long-term geochemical alteration of wellbore cement in a generic geological CO2 confinement site: tackling a difficult reactive transport modeling challenge. J. Hydrol. (Amst) 420–421, 340–359. https://doi.org/10.1016/j.jhydrol.2011.12.026.

Gupta, M., Sharma, M., Bishnoi, S., 2022. Multiscale modelling of uniaxial compressive stress-strain behaviour of concrete using analytical homogenisation and damage mechanics. Mech. Mater. 173, 104430. https://doi.org/10.1016/j.mechmat.2022.104430.

Gupta, M., Igarashi, G., Takahashi, Y., Ishida, T., 2023a. Multiscale chemo-mechanical modeling of concrete expansion with free lime-based expansive additives under restraint conditions. Cem. Concr. Compos. 141, 105126. https://doi.org/10.1016/j.cemconcomp.2023.105126.

Gupta, M., Igarashi, G., Takahashi, Y., Ishida, T., 2023b. Multiscale expansion modeling of concrete with free lime-based expansive additives under isotropic conditions using poromechanics. J. Build. Eng. 77, 107554. https://doi.org/10.1016/j.jobe.2023.107554.

Gupta, M., Qiu, X., Omran, M., Chen, Y., Khalifeh, M., Ye, G., 2025. Reaction and microstructure development of one-part geopolymer for wellbore applications – An experimental and numerical study. Cem. Concr. Res. 188, 107738. https://doi.org/10.1016/j.cemconres.2024.107738.

Hajiabadi, S.H., Bedrikovetsky, P., Borazjani, S., Mahani, H., 2021. Well injectivity during CO2 geosequestration: a review of hydro-physical, chemical, and geomechanical effects. Energy Fuels 35, 9240–9267.

Hajiabadi, S.H., Khalifeh, M., van Noort, R., Silva, P.H., Moreira, Santos, 2023a. Review on geopolymers as wellbore sealants: state of the art optimization for CO $_2$ exposure and perspectives. ACS Omega 8, 23320–23345. https://doi.org/10.1021/acsomega.3c01777.

Hajiabadi, S.H., Khalifeh, M., Van Noort, R., Moreira, P.H.S.S., 2023b. Effect of magnesium-bearing additives on the properties of a granite-based geopolymer sealant for CCS. In: 84th EAGE Annual Conference & Exhibition. European Association of Geoscientists & Engineers, pp. 1–5. https://doi.org/10.3997/2214-4609.202310742.

Hajiabadi, S.H., Khalifeh, M., van Noort, R., 2023c. Multiscale insights into mechanical performance of a granite-based geopolymer: unveiling the micro to macro behavior. Geoenergy Sci. Eng. 231, 212375. https://doi.org/10.1016/j.geoen.2023.212375.

Hajiabadi, S.H., Khalifeh, M., van Noort, R., 2024a. Stability analysis of a granite-based geopolymer sealant for CO2 geosequestration: in-situ permeability and mechanical behavior while exposed to brine. Cem. Concr. Compos. 149, 105511. https://doi.org/10.1016/j.cemconcomp.2024.105511.

Hajiabadi, H., Li, K., Pluymakers, A., van Noort, R., Khalifeh, M., 2024b. Exploring the durability of a granite-based geopolymer sealant for carbon capture and storage: evaluating sealing performance under thermal shocks in brine environment. In: Proceedings of the 17th Greenhouse Gas Control Technologies Conference (GHGT-17).

Hajiabadi, S.H., Khalifeh, M., van Noort, R., 2025. Durability assessment of a granite-based one-part geopolymer system exposed to CO2-water conditions: implications for CO2 geosequestration. Geoenergy Sci. Eng. 252, 213919. https://doi.org/10.1016/j.geoen.2025.213919.

Hall, C., 2019. Capillary imbibition in cement-based materials with time-dependent permeability. Cem. Concr. Res. 124, 105835.

Huang, H., 2014. Thermodynamics of Autogenous Self-Healing in Cementitious Materials. Delft University of Technology, Delft.

Iyer, J., Lackey, G., Edvardsen, L., Bean, A., Carroll, S.A., Huerta, N., Smith, M.M., Torsæter, M., Dilmore, R.M., Cerasi, P., 2022. A review of well integrity based on field experience at carbon utilization and storage sites. Int. J. Greenhouse Gas Control 113. https://doi.org/10.1016/j.ijggc.2021.103533.

N. Jacquemet, F. des S. et al. 54 (France) Nancy-1 Univ. Henri Poincare, well materials durability in case of carbon dioxide and hydrogen sulphide geological sequestration, (2025).

Ke, X., Bernal, S.A., Provis, J.L., Lothenbach, B., 2020. Thermodynamic modelling of phase evolution in alkali-activated slag cements exposed to carbon dioxide. Cem. Concr. Res. 136, 106158. https://doi.org/10.1016/j.cemconres.2020.106158.

Khalifeh, M., Todorovic, J., Vrålstad, T., Saasen, A., Hodne, H., 2017. Long-term durability of rock-based geopolymers aged at downhole conditions for oil well cementing operations. J. Sustain. Cem. Based. Mater. 6, 217–230. https://doi.org/10.1080/21650373.2016.1196466.

Kiran, R., Teodoriu, C., Dadmohammadi, Y., Nygaard, R., Wood, D., Mokhtari, M., Salehi, S., 2017. Identification and evaluation of well integrity and causes of failure of well integrity barriers (A review). J. Nat. Gas Sci. Eng. 45, 511–526. https://doi.org/10.1016/j.jngse.2017.05.009.

Kulik, D.A., Wagner, T., Dmytrieva, S.V., Kosakowski, G., Hingerl, F.F., Chudnenko, K.V., Berner, U.R., 2012. GEM-Selektor geochemical modeling package: revised algorithm and GEMS3K numerical kernel for coupled simulation codes. Comput. Geosci. https://doi.org/10.1007/s10596-012-9310-6.

Löher, M., Ukrainczyk, N., Bogner, A., Hirsch, A., Dehn, F., Koenders, E., 2025. Reactive transport modeling of acetic acid-induced degradation in portland cement paste. Cem. Concr. Res. 187, 107704. https://doi.org/10.1016/j.cemconres.2024.107704.

Lasaga, A.C., 1981. Chapter 4. TRANSITION State theory. Kinetics of Geochemical Processes. De Gruyter, pp. 135–170. https://doi.org/10.1515/9781501508233-008.

Li, L., Mei, R., Klausner, J.F., 2013. Multiple-relaxation-time lattice Boltzmann model for the axisymmetric convection diffusion equation. Int. J. Heat Mass Transf. 67, 338–351. https://doi.org/10.1016/j.ijheatmasstransfer.2013.08.039.

Liu, X., Chen, H., Cheng, W., Li, Y., Zhao, Y., Zhu, Y., Zeng, H., 2025a. Occurrence states and transport behavior of crude oil in different permeability oil reservoirs during depletion development. Geoenergy Sci. Eng. 252, 213944. https://doi.org/10.1016/j.geoen.2025.213944.

Liu, X., Chen, H., Li, Y., Zhu, Y., Liao, H., Zhao, Q., Zhou, X., Zeng, H., 2025b. Oil production characteristics and CO2 storage mechanisms of CO2 flooding in ultra-low permeability sandstone oil reservoirs. Pet. Explor. Dev. 52, 196–207. https://doi.org/10.1016/S1876-3804(25)60014-0.

Lothenbach, B., Kulik, D.A., Matschei, T., Balonis, M., Baquerizo, L., Dilnesa, B., Miron, G.D., Myers, R.J., 2019. Cemdata18: a chemical thermodynamic database for hydrated Portland cements and alkali-activated materials. Cem. Concr. Res. 115, 472–506. https://doi.org/10.1016/j.cemconres.2018.04.018.

Ma, B., Lothenbach, B., 2020a. Synthesis, characterization, and thermodynamic study of selected Na-based zeolites. Cem. Concr. Res. 135, 106111. https://doi.org/10.1016/j.cemconres.2020.106111.

Ma, B., Lothenbach, B., 2020b. Thermodynamic study of cement/rock interactions using experimentally generated solubility data of zeolites. Cem. Concr. Res. 135, 106149. https://doi.org/10.1016/j.cemconres.2020.106149.

Ma, B., Lothenbach, B., 2021. Synthesis, characterization, and thermodynamic study of selected K-based zeolites. Cem. Concr. Res. 148, 106537. https://doi.org/10.1016/j.cemconres.2021.106537.

Marty, N.C.M., Tournassat, C., Burnol, A., Giffaut, E., Gaucher, E.C., 2009. Influence of reaction kinetics and mesh refinement on the numerical modelling of concrete/clay interactions. J Hydrol (Amst) 364, 58–72. https://doi.org/10.1016/j.jhydrol.2008.10.013.

Marty, N.C.M., Grangeon, S., Warmont, F., Lerouge, C., 2015. Alteration of nanocrystalline calcium silicate hydrate (C-S-H) at pH 9.2 and room temperature: a combined mineralogical and chemical study. Mineral. Mag. 79, 437–458. https://doi.org/10.1180/minmag.2015.079.2.20.

Nasvi, M.C.M., Ranjith, P.G., Sanjayan, J., Haque, A., Li, X., 2014. Mechanical behaviour of wellbore materials saturated in brine water with different salinity levels. Energy 66, 239–249. https://doi.org/10.1016/j.energy.2013.12.003.

Nasvi, M.C.M., Rathnaweera, T.D., Padmanabhan, E., 2016. Geopolymer as well cement and its mechanical integrity under deep down-hole stress conditions: application for carbon capture and storage wells. Geomechan. Geophy. Geo-Energy Geo-Resour. 2, 245–256. https://doi.org/10.1007/s40948-016-0034-2.

Perry, J.H., 1950. Chemical engineers' handbook.

Raoof, A., Nick, H.M., Wolterbeek, T.K.T., Spiers, C.J., 2012a. Pore-scale modeling of reactive transport in wellbore cement under CO2 storage conditions. Int. J. Greenhouse Gas Control 11, S67–S77. https://doi.org/10.1016/j.ijggc.2012.09.012.

Raoof, A., Nick, H.M., Wolterbeek, T.K.T., Spiers, C.J., 2012b. Pore-scale modeling of reactive transport in wellbore cement under CO2 storage conditions. Int. J. Greenhouse Gas Control 11, S67–S77. https://doi.org/10.1016/j.ijggc.2012.09.012.

Raza, A., Rezaee, R., Gholami, R., Rasouli, V., Bing, C.H., Nagarajan, R., Hamid, M.A., 2015. Injectivity and quantification of capillary trapping for CO 2 storage: a review of influencing parameters. J. Nat. Gas Sci. Eng. 26, 510–517. https://doi.org/10.1016/j.jngse.2015.06.046.

Redlich, O., Kwong, J.N.S., 1949. On the thermodynamics of solutions. V. An equation of state. Fugacities of gaseous solutions. Chem. Rev. 44, 233–244.

Samarakoon, M.H., Ranjith, P.G., Wanniarachchi, W.A.M., 2022. Properties of well cement following carbonated brine exposure under HTHP conditions: a comparative study of alkali-activated and class G cements. Cem. Concr. Compos. 126, 104342. https://doi.org/10.1016/j.cemconcomp.2021.104342.

Spycher, N., Pruess, K., Ennis-King, J., 2003. CO2-H2O mixtures in the geological sequestration of CO2. I. Assessment and calculation of mutual solubilities from 12 to 100 °C and up to 600 bar. Geochim. Cosmochim. Acta 67, 3015–3031. https://doi.org/10.1016/S0016-7037(03)00273-4.

Steefel, C.I., Yabusaki, S.B., 2000. OS3D/GIMRT Software for Modeling Multicomponent-Multidimensional Reactive Transport. Pacific Northwest National Lab.(PNNL), Richland, WA (United States).

Steefel, C.I., Appelo, C.A.J., Arora, B., Jacques, D., Kalbacher, T., Kolditz, O., Lagneau, V., Lichtner, P.C., Mayer, K.U., Meeussen, J.C.L., Molins, S., Moulton, D., Shao, H., Šimůnek, J., Spycher, N., Yabusaki, S.B., Yeh, G.T., 2015. Reactive transport codes for subsurface environmental simulation. Comput. Geosci. 19, 445–478. https://doi.org/10.1007/s10596-014-9443-x.

Stocker, T., 2014. Climate Change 2013: the Physical Science basis: Working Group I Contribution to the Fifth Assessment Report of the Intergovernmental Panel on Climate Change. Cambridge university press.

Trapote-Barreira, A., Cama, J., Soler, J.M., 2014. Dissolution kinetics of C–S–H gel: flow-through experiments. Physics Chem. Earth, Parts A/B/C 70–71, 17–31. https://doi.org/10.1016/j.pce.2013.11.003.

Turner, L.K., Collins, F.G., 2013. Carbon dioxide equivalent (CO2-e) emissions: a comparison between geopolymer and OPC cement concrete. Constr. Build. Mater. 43, 125–130. https://doi.org/10.1016/j.conbuildmat.2013.01.023.

K. Van Breugel, Simulation of hydration and formation of structure in hardening cement-based materials., (1993).

van der Lee, J., De Windt, L., Lagneau, V., Goblet, P., 2003. Module-oriented modeling of reactive transport with HYTEC. Comput. Geosci. 29, 265–275. https://doi.org/10.1016/S0098-3004(03)00004-9.

van Noort, R., Gupta, M., Hajiabadi, H., Khalifeh, M., Kvassnes, A., Li, K., Pluymakers, A., Starrs, G., Svenningsen, G., Ye, G., Suryanto, B., 2024. Development and testing of novel cement designs for enhanced CCS well integrity. In: Proceedings of the 17th Greenhouse Gas Control Technologies Conference (GHGT-17).

van Noort, R., Svenningsen, G., Li, K., Pluymakers, A., 2025a. Exposure of five cementitious sealant materials to wet supercritical CO2 and CO2-saturated water under simulated downhole conditions. Int. J. Greenhouse Gas Control 144, 104380. https://doi.org/10.1016/j.ijggc.2025.104380.

van Noort, R., Svenningsen, G., Li, K., 2025b. Experimental study on the impact of H2S and H2SO4 in CO2 on five different sealant compositions under conditions relevant for geological CO2-storage. Geoenergy Sci. Eng. 253, 214005. https://doi.org/10.1016/j.geoen.2025.214005.

Wagner, T., Kulik, D.A., Hingerl, F.F., Dmytrieva, S.V., 2012. GEM-Selektor geochemical modeling package: tSolMod library and data interface for multicomponent phase models. Canadian Mineralogist 50, 1173–1195.

Wennersten, R., Sun, Q., Li, H., 2015. The future potential for Carbon Capture and Storage in climate change mitigation – an overview from perspectives of technology, economy and risk. J. Clean. Prod. 103, 724–736. https://doi.org/10.1016/j.jclepro.2014.09.023.

Xu, T., Sonnenthal, E., Spycher, N., Pruess, K., 2006. TOUGHREACT—A simulation program for non-isothermal multiphase reactive geochemical transport in variably saturated geologic media: applications to geothermal injectivity and CO2 geological sequestration. Comput. Geosci. 32, 145–165. https://doi.org/10.1016/j.cageo.2005.06.014.

Xu, T., Zheng, L., Tian, H., 2011a. Reactive transport modeling for CO2 geological sequestration. J. Pet. Sci. Eng. 78, 765–777. https://doi.org/10.1016/j.petrol.2011.09.005.

Xu, T., Spycher, N., Sonnenthal, E., Zhang, G., Zheng, L., Pruess, K., 2011b. TOUGHREACT Version 2.0: a simulator for subsurface reactive transport under non-isothermal multiphase flow conditions. Comput. Geosci. 37, 763–774. https://doi.org/10.1016/j.cageo.2010.10.007.

Xuan, Y.M., Zhao, K., Li, Q., 2010. Investigation on mass diffusion process in porous media based on Lattice Boltzmann method. Heat Mass Transfer 46, 1039–1051. https://doi.org/10.1007/s00231-010-0687-2.

G. Ye, Experimental study and numerical simulation of the development of the microstructure and permeability of cementitious materials, (2003).

Yoshida, H., Nagaoka, M., 2010. Multiple-relaxation-time lattice Boltzmann model for the convection and anisotropic diffusion equation. J. Comput. Phys. 229, 7774–7795. https://doi.org/10.1016/j.jcp.2010.06.037.

Zoski, C.G., 2006. Handbook of Electrochemistry. Elsevier.

Zuo, Y., Ye, G., 2021. GeoMicro3D: a novel numerical model for simulating the reaction process and microstructure formation of alkali-activated slag. Cem. Concr. Res. 141, 106328. https://doi.org/10.1016/j.cemconres.2020.106328.